DC-Link High-Frequency Current Ripple Elimination Strategy for MMCs Using Phase-Shifted Double-Group Multicarrier-Based Phase-Disposition PWM

Qiang Yu, Fujin Deng, *Senior Member, IEEE*, Chengkai Liu, Jifeng Zhao, Frede Blaabjerg, *Fellow, IEEE*, and Sayed Abulanwar, *Member, IEEE*

***Abstract*—The active circulating current suppression may cause high-frequency current ripple in the dc link of modular multilevel converters (MMCs). In this article, a phase-shifted double-group multicarrier-based phase-disposition pulsewidth modulation strategy is proposed to eliminate the dc-link high-frequency current ripple of MMCs, where the fundamental frequency component and the second-order component of the arm reference are modulated, respectively, by two groups of carriers. By shifting the phase angles of double-group multicarrier in each carrier period, the high-frequency current ripple injected into the dc link of MMCs can be eliminated. The proposed strategy not only eliminates the dc-link current ripple, but also extends the active and reactive power region of MMCs in comparison with the existing method. Simulation and experimental studies are conducted, and their results verify the effectiveness of the proposed strategy.**

***Index Terms*—Control strategy, dc-link current ripple, modular multilevel converters (MMCs), modulation strategy.**

I. Introduction

THE modular multilevel converter (MMC) was first proposed in 2003 [1] and has been increasingly attractive in both medium- and high-voltage applications [2]–[6]. Compared with two- or three-level converters, the MMC has many irreplaceable advantages and salient features such as high modularity and high efficiency [7]–[9].

Manuscript received July 9, 2020; revised October 27, 2020; accepted December 22, 2020. Date of publication January 5, 2021; date of current version May 5, 2021. This work was supported in part by the National Natural Science Foundation of China under Project 61873062 and in part by the Natural Science Foundation of Jiangsu Province under Project BK20180395. Recommended for publication by Associate Editor G. Konstantinou. *(Corresponding author: Fujin Deng.)*

Qiang Yu, Chengkai Liu, and Jifeng Zhao are with the School of Electrical Engineering, Southeast University, Nanjing 210096, China (e-mail: yyuqiang@163.com; lckisafish@163.com; 230189827@seu.edu.cn).

Fujin Deng is with the School of Electrical Engineering and Jiangsu Key Laboratory of Smart Grid Technology and Equipment, Southeast University, Nanjing 210096, China (e-mail: fdeng@seu.edu.cn).

Frede Blaabjerg is with the Department of Energy Technology, Aalborg University, 9220 Aalborg, Denmark (e-mail: fbl@et.aau.dk).

Sayed Abulanwar is with the Electrical Engineering Department, Faculty of Engineering, Mansoura University, Mansoura 35516, Egypt (e-mail: abulanwar@mans.edu.eg).

This article has supplementary material provided by the authors and color versions of one or more figures available at https://doi.org/10.1109/TPEL.2021.3049150.

Digital Object Identifier 10.1109/TPEL.2021.3049150

The power quality is one of the important issues for the MMC. Some works have focused on the ac side harmonics [10], [11] and inner current harmonics [12], [13] of the MMC. Recently, the dc-link current ripple of the MMC is also given much attention [14]–[21]. Due to modulation schemes, unbalanced grid conditions, etc., the low-frequency or high-frequency harmonic current would be produced in three phases and the zero-sequence component would be injected into the dc link of the MMC to cause low-frequency or high-frequency current ripple, which may deteriorate the dc-link power quality of the MMC. It will increase device voltage stress [16], cause high-frequency noise [20], [21], affect the equipment connected to the dc link [21], and may increase the dc filter cost [19]. Therefore, it is of great significance to suppress the dc-link current ripple.

To date, some researches have been conducted for reducing the dc-link low-frequency current ripple of the MMC. Tu *et al.* [14] present a supplementary dc voltage ripple suppressing controller to eliminate the dc-link low-frequency current ripple. Wang *et al.* [15] present three improved strategies based on proportional resonant controllers to eliminate both circulating current and dc-link low-frequency current ripple of the MMC. Dekka *et al.* [16] present a model-predictive control method to minimize the dc-link low-frequency current ripple of the MMC under the unbalanced grid voltage conditions.

Recently, some studies have focused on the dc-link high-frequency current ripple of the MMC. Deng and Chen [17] analyze the arm current high-frequency harmonics at switching frequency of the MMC under improved phase-shifted-carrier pulsewidth modulation (PWM), which would be injected into the dc link of the MMC and causes high-frequency current ripple. Deng and Chen [18] further propose a dc-link high-frequency current ripple elimination method for [17] by regulating the phase-shifted angles of the carriers. On the other hand, the active circulating current suppression would also cause the dc-link high-frequency current ripple of the MMC [19]–[21]. Li *et al.* [19] propose an arm inductance selection rule for the MMC to reduce the circulating current harmonics and the dc-link high-frequency current ripple at the switching frequency produced by the active circulating current suppression. Li *et al.* [20] propose a topology employing a circulating current suppression

inverter and replacing the arm inductors with three-winding transformers, which could suppress the circulating current and improve the dc-link power quality. However, increased hardware investment is required in both [19] and [20]. Deng *et al.* [21] analyze the dc-link current ripple of MMCs caused by the active circulating current suppression under phase-disposition (PD) PWM and presents a variable carrier phase-shifted angle control strategy to reduce the dc-link high-frequency current ripple for the MMC. However, it reduces the power operation region of the MMC.

This article proposes a phase-shifted double-group multicarrier (DGM) based PD-PWM strategy to eliminate the dc-link high-frequency current ripple, which improves the dc-link power quality, reduces high-frequency noise, and avoids the harm to the equipment connected to the dc link of the MMC. In the proposed strategy, the fundamental frequency component and the second-order component of the arm reference are modulated by two groups of carriers, respectively. The primary contributions of this article are as follows.

1) The dc-link high-frequency current ripple is eliminated through regulating the phase angle of carriers for each phase of the MMC.
2) The operating regions of the active power and reactive power under the proposed strategy and strategy in [21] are analyzed in detail, respectively, which is related to the fundamental-frequency component and the second-order component of the reference.
3) The proposed strategy can not only eliminate the dc-link high-frequency current ripple but also extends the active power and reactive power operating region for the MMC in comparison with [21].

The rest of this article is organized as follows. Section II presents the principle of MMCs. Section III analyzes the dc-link high-frequency current ripple of MMCs under PD-PWM. Section IV proposes the dc-link high-frequency current ripple elimination strategy. Section V analyzes the power region of the MMC under the proposed strategy. Section VI compares the proposed strategy with the existing strategy. The simulation and experimental results are presented in Sections VII and VIII, respectively, to show the effectiveness of the proposed strategy. Finally, Section IX concludes this article.

II. Description of MMCs

Fig. 1 shows a three-phase MMC tied to a grid. Each phase of the MMC has an upper arm and a lower arm. Each arm consists of N identical submodules (SMs) and an inductor L_s. Each SM includes a storage capacitor C and two switches T_1, T_2. When T_1 is on and T_2 is off, the C is inserted into the circuit; when T_1 is off and T_2 is on, the C is bypassed from circuit [5].

In Fig. 1, the three-phase grid voltages are defined as

$$\begin{cases} e_a = E_m \sin(\omega_0 t) \\ e_b = E_m \sin(\omega_0 t - 2\pi/3) \\ e_c = E_m \sin(\omega_0 t + 2\pi/3) \end{cases} \tag{1}$$

where E_m is the amplitude of the grid voltage and ω_0 is the fundamental angular frequency. According to [10] and [22], the

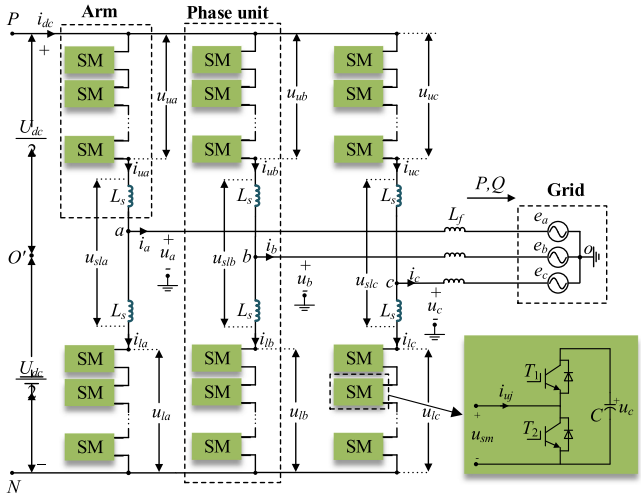

Fig. 1. Three-phase MMC.

dynamics of the MMC can be described as

$$\begin{cases} u_{ea} = (u_{la} - u_{ua})/2 = L di_a/dt + e_a \\ u_{eb} = (u_{lb} - u_{ub})/2 = L di_b/dt + e_b \\ u_{ec} = (u_{lc} - u_{uc})/2 = L di_c/dt + e_c \end{cases} \tag{2}$$

where u_{ea}, u_{eb}, u_{ec} are the ac electromotive forces (EMFs) of MMCs. u_{uj} and u_{lj} are the total SM output voltage in the upper and lower arm of phase j ($j = a, b, c$), respectively; $L = L_f + L_s/2$. L_f is the filter inductance at the ac side.

Suppose that the active power and reactive power in Fig. 1 are P and Q, respectively, the three-phase grid current can be obtained as

$$\begin{cases} i_a = I_m \sin(\omega_0 t - \varphi) \\ i_b = I_m \sin(\omega_0 t - \varphi - 2\pi/3) \\ i_c = I_m \sin(\omega_0 t - \varphi + 2\pi/3) \end{cases} \tag{3}$$

with

$$\begin{cases} I_m = 2\sqrt{P^2 + Q^2}/3E_m \\ \varphi = \arctan(Q/P). \end{cases} \tag{4}$$

Substituting (1), (3), and (4) into (2), the EMF of the MMC can be written as

$$\begin{cases} u_{ea} = U_e \sin(\omega_0 t + \delta) \\ u_{eb} = U_e \sin(\omega_0 t + \delta - 2\pi/3) \\ u_{ec} = U_e \sin(\omega_0 t + \delta + 2\pi/3) \end{cases} \tag{5}$$

with

$$\begin{cases} U_e = \frac{1}{3E_m}\sqrt{(2\omega_0 LP)^2 + \left(3{E_m}^2 - 2\omega_0 LQ\right)^2} \\ \delta = \arctan\left(\frac{\omega_0 LP}{3{E_m}^2/2 - \omega_0 LQ}\right). \end{cases} \tag{6}$$

III. DC-Link High-Frequency Current Ripple of MMCs Under PD-PWM

A. Circulating Current Suppression and PD-PWM

Fig. 2 shows the active circulating current suppression control [13] and PD-PWM [21], where the upper arm reference y_{uj} and

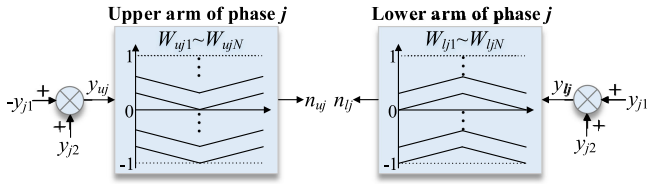

Fig. 2. Circulating current suppression and PD-PWM.

lower arm reference y_{lj} of the MMC can be written as

$$\begin{cases} y_{uj} = & -y_{j1} & +y_{j2} \\ y_{lj} = & y_{j1} & +y_{j2} \\ & \underset{\text{component}}{\text{Fundamental}} & \underset{\text{component}}{\text{Second-order}} \end{cases} \tag{7}$$

with

$$\begin{cases} y_{a1} = m_1 \sin(\omega_0 t + \alpha_1) \\ y_{b1} = m_1 \sin(\omega_0 t - 2\pi/3 + \alpha_1) \\ y_{c1} = m_1 \sin(\omega_0 t + 2\pi/3 + \alpha_1) \end{cases} \tag{8}$$

$$\begin{cases} y_{a2} = m_2 \sin(2\omega_0 t + \alpha_2) \\ y_{b2} = m_2 \sin(2\omega_0 t + 2\pi/3 + \alpha_2) \\ y_{c2} = m_2 \sin(2\omega_0 t - 2\pi/3 + \alpha_2) \end{cases} \tag{9}$$

where m_1 and α_1 are the modulation index and phase angle of the fundamental frequency component, respectively. m_2 and α_2 are the modulation index and phase angle of the second-order component, respectively.

In Fig. 2, the y_{uj} is compared with N number of triangular carriers W_{uj1}~W_{ujN} to yield the number n_{uj} of inserted SMs in the upper arm, where W_{uj1}~W_{ujN} are displaced evenly between –1 and 1. The y_{lj} is compared with N number of triangular carriers W_{lj1}~W_{ljN} to yield the number n_{lj} of inserted SMs in the lower arm, where W_{lj1}~W_{ljN} are displaced evenly between –1 and 1. W_{uj1}~W_{ujN} and W_{lj1}~W_{ljN} are phase shifted by π.

B. DC-Link High-Frequency Current Ripple

Suppose that the capacitor voltages are kept the same as $U_{\rm dc}/N$ with voltage-balancing control [8], the total arm inductor voltage u_{slj} in phase j, as shown in Fig. 1, is

$$u_{slj} = U_{\rm dc} - (u_{uj} + u_{lj}) \tag{10}$$

with

$$\begin{cases} u_{uj} = n_{uj} U_{\rm dc}/N \\ u_{lj} = n_{lj} U_{\rm dc}/N \end{cases} \tag{11}$$

where $U_{\rm dc}$ is the dc-link voltage of the MMC.

Fig. 3(a) and (b) shows two cases of PD-PWM in one carrier period for the MMC when $y_{j2} > 0$ and $y_{j2} < 0$, respectively.

1) $y_{j2} > 0$: The $-y_{j1}$ crosses the Kth carrier $W_{uj\rm K}$ for the upper arm and the y_{j1} crosses the $(N–K+1)$th carrier $W_{lj(N-{\rm K}+1)}$ for the lower arm. Due to the positive y_{j2}, the sum of n_{uj} and n_{lj} is between N and $(N+1)$. According to (10), the total arm inductor voltage u_{slj} has two negative voltage pulses in one carrier period.
2) $y_{j2} < 0$: The $-y_{j1}$ crosses $W_{uj\rm K}$ for the upper arm and the y_{j1} crosses $W_{lj(N-{\rm K}+1)}$ for the lower arm. Due to the negative y_{j2}, the sum of n_{uj} and n_{lj} is between $(N–1)$ and N. According to (10), the total arm inductor voltage u_{slj} has two positive voltage pulses in one carrier period.

According to the geometrical relationship in Fig. 3, θ_j and the θ_{mj} of the voltage u_{slj} can be obtained as

$$\begin{cases} \theta_j = -y_{j2} \cdot N \cdot \pi \\ \theta_{mj} = \bmod(1 - y_{j1}, 2/N) \cdot N \cdot \pi. \end{cases} \tag{12}$$

The voltages u_{sla}, u_{slb}, u_{slc} would cause high-frequency current in phases A, B, and C, respectively, which would be injected into the dc link of the MMC [21]. With the Fourier series expansion of u_{slj}, the caused current ripple in the dc link of the MMC can be expressed as

$$\begin{aligned} \tilde{i}_{\rm dc} &= \int \left(\frac{u_{sla}}{2L_s} + \frac{u_{slb}}{2L_s} + \frac{u_{slc}}{2L_s}\right) dt \\ &= \frac{U_{\rm dc}}{N\pi^2 L_s f_c} \sum_{i=1}^{\infty} \left\{ \frac{1}{i^2} \cos(i\pi) \left[\sin\left(\frac{i\theta_a}{2}\right) \cos\left(\frac{i\theta_{ma}}{2}\right) \right.\right. \\ &\quad + \sin\left(\frac{i\theta_b}{2}\right) \cos\left(\frac{i\theta_{mb}}{2}\right) \\ &\quad \left.\left. + \sin\left(\frac{i\theta_c}{2}\right) \cos\left(\frac{i\theta_{mc}}{2}\right) \right] \sin(2i\pi f_c t) \right\} \end{aligned} \tag{13}$$

where f_c is the carrier frequency and i is the index of the summation terms in Fourier series expansion. Thus, the high-frequency current ripple would be caused in the dc link of the MMC.

IV. Proposed DC-Link High-Frequency Current Ripple Elimination Strategy

A. Proposed DGM-Based PD-PWM

According to the superposition principle and area equivalent theory of the PWM [23], a DGM-based PD-PWM strategy is proposed, as shown in Fig. 4, where the arm reference in (7) is divided into two parts. One is the fundamental component $\pm y_{j1}$, which is modulated by N number of carriers. The other one is the second-order component y_{j2}, which is modulated by M carriers. The M is

$$M = \begin{cases} N, & \text{when } N \text{ is even} \\ N+1, & \text{when } N \text{ is odd.} \end{cases} \tag{14}$$

1) DGM-Based PD-PWM for the Upper Arm of Phase j: The $-y_{j1}$ is compared with N carriers $W_{{\rm I}\_uj1}$~$W_{{\rm I}\_ujN}$ to generate the voltage level n_{uj1}, where $W_{{\rm I}\_uj1}$~$W_{{\rm I}\_ujN}$ are displaced evenly between –1 and 1 and the phase angle of the $W_{{\rm I}\_uj1}$~$W_{{\rm I}\_ujN}$'s lowest point is θ_{sj}. The y_{j2} is compared with M carriers $W_{{\rm II}\_uj1}$~$W_{{\rm II}\_ujM}$, where $W_{{\rm II}\_uj1}$~$W_{{\rm II}\_ujM}$ are displaced evenly between –1 and 1 and the phase angle of the $W_{{\rm II}\_uj1}$~$W_{{\rm II}\_ujM}$'s highest point is θ_{sj}. Then, $M/2$ is subtracted by the comparison result of y_{j2} and $W_{{\rm II}\_uj1}$~$W_{{\rm II}\_ujM}$ to generate the voltage level n_{uj2}. The total voltage level produced in the upper arm is $n_{uj} = n_{uj1} + n_{uj2}$.

2) DGM-Based PD-PWM for the Lower Arm of Phase j: The y_{j1} is compared with N carriers $W_{{\rm I}\_lj1}$~$W_{{\rm I}\_ljN}$ to generate the voltage level n_{lj1}, where the $W_{{\rm I}\_lj1}$~$W_{{\rm I}\_ljN}$ are displaced evenly between –1 and 1 and the phase angle of the $W_{{\rm I}\_lj1}$~$W_{{\rm I}\_ljN}$'s

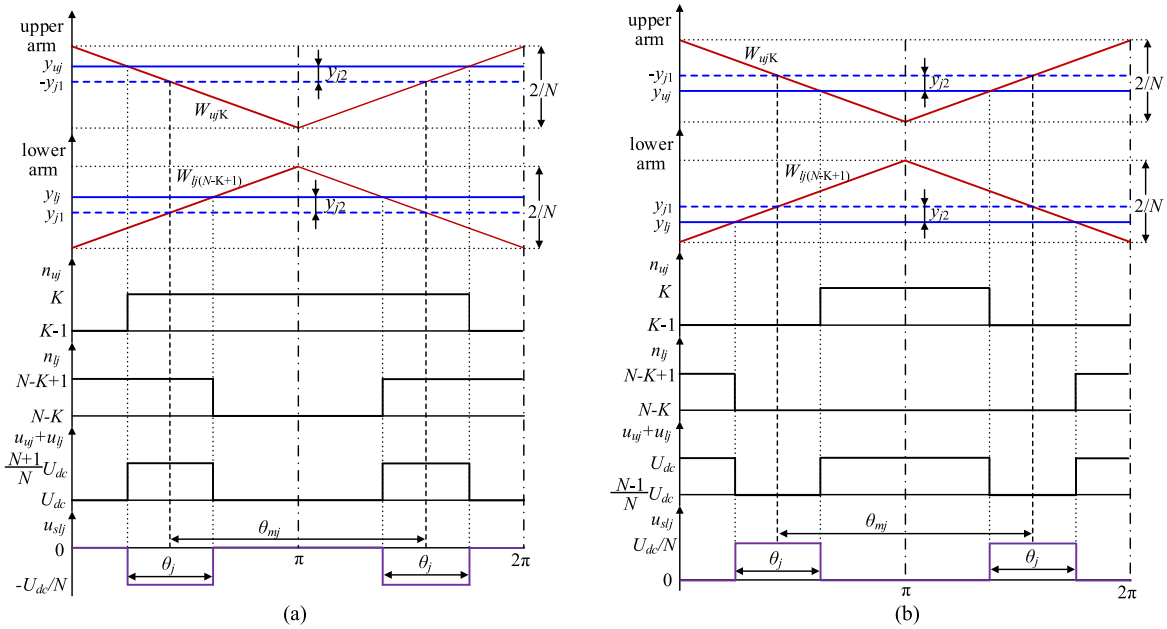

Fig. 3. PD-PWM for MMCs under circulating current control. (a) $y_{j2} > 0$. (b) $y_{j2} < 0$.

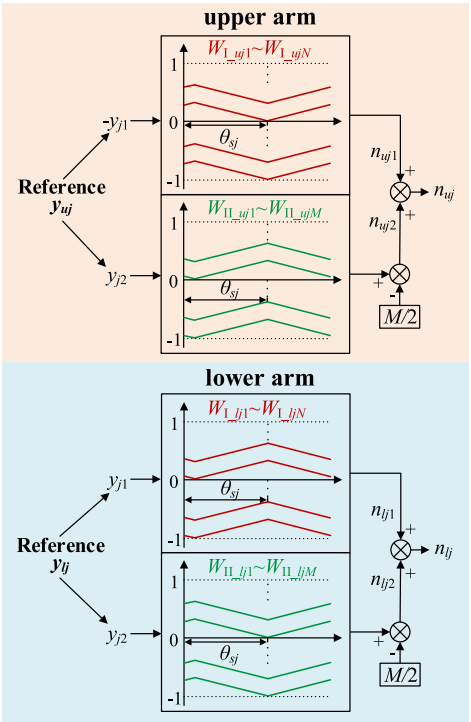

Fig. 4. Proposed modulation strategy.

highest point is θ_{sj}. The y_{j2} is compared with M carriers W_{II_lj1}~W_{II_ljM}, where W_{II_lj1}~W_{II_ljM} are displaced evenly between -1 and 1 and the phase angle of the W_{II_lj1}~W_{II_ljM}'s lowest point is θ_{sj}. Then, $M/2$ is subtracted by the comparison result of y_{j2} and W_{II_lj1}~W_{II_ljM} to generate the voltage level n_{lj2}. The total voltage level produced in the lower arm is $n_{lj} = n_{lj1} + n_{lj2}$.

B. Arm Inductor Voltage Under DGM-Based PD-PWM

Fig. 5 shows the proposed DGM-based PD-PWM. Fig. 5(a) displays the case when $y_{j2} > 0$ and Fig. 5(b) displays the case when $y_{j2} < 0$.

1) Case 1: $\mathrm{y_{j2}} > 0$*:* In the upper arm, $-y_{j1}$ crosses $W_{\mathrm{I}\_uj\mathrm{K}}$, and n_{uj1} is between K–1 and K; y_{j2} crosses the $(M/2 + S)$th carrier $W_{\mathrm{II}\_uj(M/2\,+\,S)}$, and n_{uj2} is between S–1 and S. Therefore, n_{uj} is between $K + S$–2 and $K + S$–1. In the lower arm, y_{j1} crosses $W_{\mathrm{I}\_lj(N\text{-}K\,+\,1)}$, and n_{lj1} is between N–K and N–K + 1; y_{j2} crosses $W_{\mathrm{II}\_lj(M/2\,+\,S)}$, and n_{lj2} is between S–1 and S. Therefore, n_{lj} is between N–$K + S$–1 and N–$K + S$. As a result, the sum of u_{uj} and u_{lj} is between $(N + 2S\text{–}2)U_{\mathrm{dc}}/N$ and $(N + 2S\text{–}1)U_{\mathrm{dc}}/N$. According to (10), the inductor voltage u_{slj} is between $-(2S\text{–}1)U_{dc}/N$ and $-(2S\text{–}2)U_{\mathrm{dc}}/N$.

2) Case 2: $\mathrm{y_{j2}} < 0$*:* In the upper arm, $-y_{j1}$ crosses W_{I_ujK}, and n_{uj1} is between K–1 and K; y_{j2} crosses $W_{\mathrm{II}\_uj(M/2\text{–}\mathrm{S})}$, and n_{uj2} is between $-S$–1 and $-S$. Therefore, n_{uj} is between K–S–1 and K–S. In the lower arm, y_{j1} crosses $W_{\mathrm{I}\_lj(N-\mathrm{K}\,+\,1)}$, and n_{lj1} is between N–K and N–$K + 1$; y_{j2} crosses $W_{\mathrm{II}\_lj(M/2-S)}$, and n_{lj2} is between $-S$–1 and $-S$. Therefore, n_{lj} is between N–K–S and N–K–$S + 1$. As a result, the sum of u_{uj} and u_{lj} is between $(N$–$2S$–1)U_{dc}/N and $(N$–$2S)U_{\mathrm{dc}}/N$. According to (10), the inductor voltage u_{slj} is between $2SU_{\mathrm{dc}}/N$ and $(1 + 2S)U_{\mathrm{dc}}/N$.

In Fig. 5(a) and (b), the width θ_j and the distance θ_{mj} of the inductor voltage u_{slj} can be calculated by geometrical relationship as

$$\begin{cases} \theta_j = -y_{j2} \cdot M \cdot \pi \\ \theta_{mj} = \pi. \end{cases} \tag{15}$$

Based on (9) and (15), the relationship among θ_a, θ_b, and θ_c can be obtained as

$$\theta_a + \theta_b + \theta_c = 0. \tag{16}$$

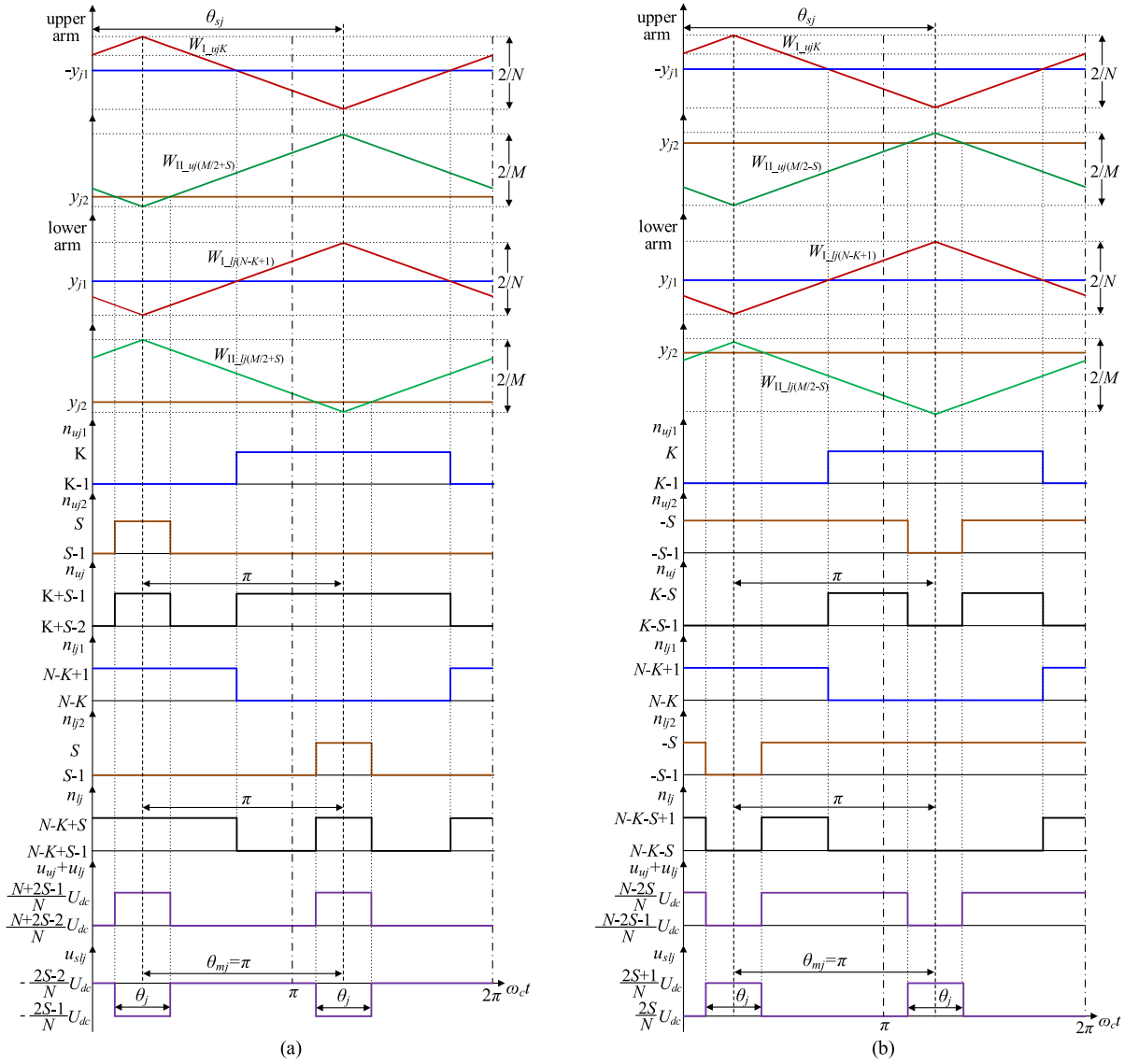

Fig. 5. Two cases of the proposed DGM-based PD-PWM. (a) $y_{j2} > 0$. (b) $y_{j2} < 0$.

C. Proposed DC-Link High-Frequency Current Ripple Elimination Strategy

A phase-shifted DGM-based PD-PWM strategy is proposed to eliminate the dc-link high-frequency current ripple. Fig. 6 shows the proposed strategy for the upper arm of phase *j*. The sorting index list K_{uj1}∼K_{ujN} for the SMs is established based on the capacitor voltages u_{cuj1}∼u_{cujN}. The number n_{uj} of inserted SMs in the arm can be obtained by the references $-y_{j1}$ and y_{j2} under the proposed DGM-based PD-PWM, where the phase-shifted angle for all carriers is θ_{sj}. According to the sorting index list and the arm current i_{uj}, n_{uj} SMs are selected to be inserted into the arm to keep the capacitor voltage balance as follows.

1) $i_{uj} > 0$: n_{uj} SMs with the lowest capacitor voltages are inserted into the arm.
2) $i_{uj} < 0$: n_{uj} SMs with the highest capacitor voltages are inserted into the arm.

Fig. 7 shows the calculation of the carriers' phase angles θ_{sa}, θ_{sb}, and θ_{sc} for phases A, B, and C, respectively. In Fig. 7, $|\theta_a|$, $|\theta_b|$, and $|\theta_c|$ corresponding to the arm inductor voltage pulses u_{sla}, u_{slb}, and u_{slc} can be calculated by y_{a2}, y_{b2}, and y_{c2} and (15). Afterward, the $|\theta_a|$, $|\theta_b|$, and $|\theta_c|$ are sorted in ascending order for the rank list $K_{\theta a}$, $K_{\theta b}$, and $K_{\theta c}$, which are between 1 and 3. The θ_{sj} of carriers in phase *j* is obtained based on $K_{\theta j}$ as follows.

1) $K_{\theta j} = 1$: θ_{sj} is π.
2) $K_{\theta j} = 2$: θ_{sj} is π–[max($|\theta_a|$, $|\theta_b|$, $|\theta_c|$)–$|\theta_j|$]/2.
3) $K_{\theta j} = 3$: θ_{sj} is π + [max($|\theta_a|$, $|\theta_b|$, $|\theta_c|$)–$|\theta_j|$]/2.

According to (15) and (16), through regulating θ_{sa}, θ_{sb}, and θ_{sc} for carriers in phases A, B, and C in each carrier period, respectively, the arm inductor voltage pulses u_{sla}, u_{slb}, u_{slc} in three phases can be counteracted as

$$u_{sla} + u_{slb} + u_{slc} = 0. \tag{17}$$

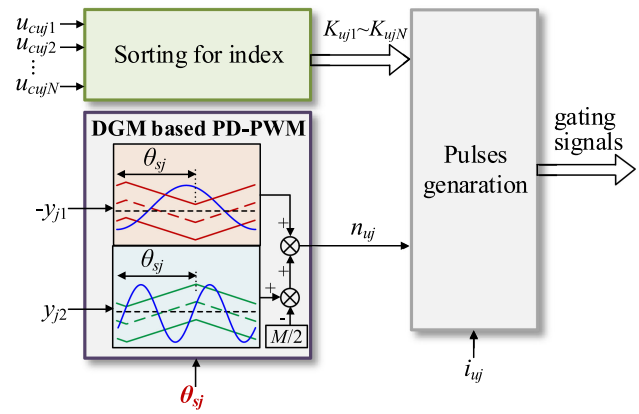

Fig. 6. Proposed dc-link high-frequency current ripple elimination strategy for the upper arm of phase *j*.

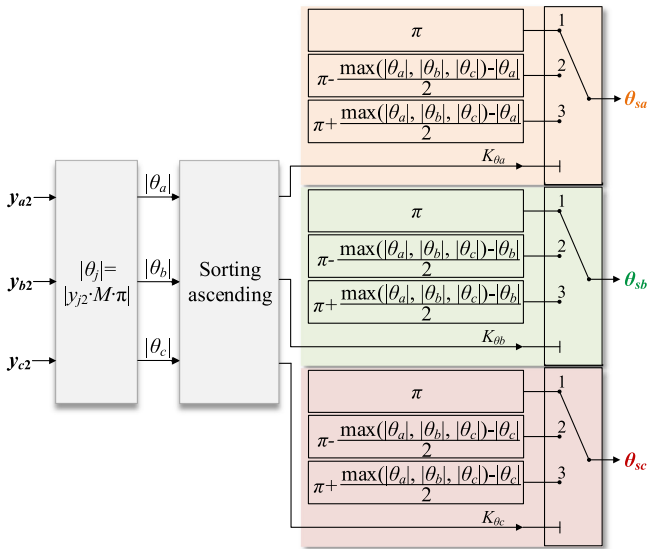

Fig. 7. Calculation of carriers' phase angle θ_{sa}, θ_{sb}, and θ_{sc} in the proposed strategy.

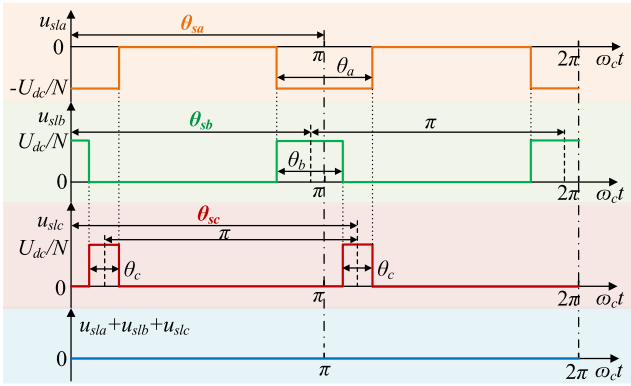

Fig. 8. Inductor voltages u_{sla}, u_{slb}, and u_{slc} under the proposed strategy.

Combining (13) and (17), the dc-link high-frequency current ripple can be eliminated by the proposed strategy. Fig. 8 shows an example of u_{sla}, u_{slb}, and u_{slc} using the proposed strategy where the sum of arm inductor voltages in phases A, B, and C is zero in a carrier period and ensures the elimination of the dc-link high-frequency current ripple.

V. Operation Region Analysis of the Proposed Strategy

A. References y_{j1} and y_{j2}

According to Fig. 4, the SM equivalent references in the upper and lower arms of phase A can be expressed as

$$\begin{cases} y_{eua} = -y_{a1} + y_{a2} \cdot M/N \\ y_{ela} = y_{a1} + y_{a2} \cdot M/N. \end{cases} \tag{18}$$

In the MMC, since the second-order harmonic circulating current is suppressed, the upper arm current i_{ua} and lower arm current i_{la} in phase A can be expressed as

$$\begin{cases} i_{ua} = i_{\rm dc}/3 + i_a/2 \\ i_{la} = i_{\rm dc}/3 - i_a/2 \end{cases} \tag{19}$$

where $i_{\rm dc}$ is the dc-link current as $i_{\rm dc} = P/U_{\rm dc}$.

According to (18), (19), and Fig. 1, the capacitor voltages u_{cua} and u_{cla} in the upper and lower arm are as follows:

$$\begin{cases} u_{cua} = \frac{1}{C}\int i_{ua} \cdot \frac{1+y_{eua}}{2} dt \\ u_{cla} = \frac{1}{C}\int i_{la} \cdot \frac{1+y_{ela}}{2} dt. \end{cases} \tag{20}$$

According to (18) and (20), the total SM output voltages u_{ua} and u_{la} in upper and lower arms can be calculated as

$$\begin{cases} u_{ua} = N u_{cua} \cdot \frac{1+y_{eua}}{2} \\ u_{la} = N u_{cla} \cdot \frac{1+y_{ela}}{2}. \end{cases} \tag{21}$$

Substituting (3), (8), (9), and (18)–(20) into (21), neglecting the high-order harmonics, u_{ua} and u_{la} can be rewritten as

$$\begin{cases} u_{ua} = U_{a0} - \underbrace{\frac{[U_{a1\_\sin}\sin(\omega_0 t) + U_{a1\_\cos}\cos(\omega_0 t)]}{\text{Fundamental component}}} \\ \qquad + \underbrace{\frac{[U_{a2\_\sin}\sin(2\omega_0 t) + U_{a2\_\cos}\cos(2\omega_0 t)]}{\text{Second-order component}}} \\ u_{la} = U_{a0} - \underbrace{\frac{[U_{a1\_\sin}\sin(\omega_0 t) + U_{a1\_\cos}\cos(\omega_0 t)]}{\text{Fundamental component}}} \\ \qquad + \underbrace{\frac{[U_{a2\_\sin}\sin(2\omega_0 t) + U_{a2\_\cos}\cos(2\omega_0 t)]}{\text{Second-order component}}} \end{cases} \tag{22}$$

with

$$\begin{aligned} U_{a0} = {} & \frac{NU_{\rm cap}}{2} + \frac{Nm_1 I_m}{16\omega_0 C}\sin(\varphi + \alpha_1) \\ & - \frac{Mm_1 m_2 I_m}{64\omega_0 C}\cos(\varphi - \alpha_1 + \alpha_2) \end{aligned} \tag{23}$$

$$U_{a1\_\sin} = \frac{N}{192\omega_0 C}\begin{bmatrix} 96\omega_0 C m_1 U_{\rm cap}\cos\alpha_1 + 24 I_m \sin\varphi \\ +16 m_1 i_{\rm dc}\sin\alpha_1 + 3m_1^2 I_m \sin\varphi \\ +4(M/N)^2 m_2^2 I_m \sin\varphi \\ -4\frac{M}{N} m_1 m_2 i_{\rm dc}\cos(-\alpha_1 + \alpha_2) \end{bmatrix} \tag{24}$$

$$U_{a1\_\cos} = \frac{N}{192\omega_0 C}\begin{bmatrix} 96\omega_0 C m_1 U_{\rm cap}\sin\alpha_1 + 24 I_m \cos\varphi \\ -16 m_1 i_{\rm dc}\cos\alpha_1 + 3m_1^2 I_m \cos\varphi \\ -4(M/N)^2 m_2^2 I_m \cos\varphi \\ -4\frac{M}{N} m_1 m_2 i_{\rm dc}\sin(-\alpha_1 + \alpha_2) \end{bmatrix} \tag{25}$$

Fig. 9. Calculation for references y_{j1} and y_{j2} under the proposed strategy.

$$U_{a2\_\sin}=\frac{N}{96\omega_0 C}\begin{bmatrix}\frac{M}{N}48\omega_0 C m_2 U_{\rm cap}\cos\alpha_2\\ +9m_1 I_m\cos(\varphi-\alpha_1)\\ +4\frac{M}{N}m_2 i_{\rm dc}\sin\alpha_2-4m_1^2 i_{\rm dc}\cos 2\alpha_1\\ -3\frac{M}{N}m_1 m_2 I_m\sin(\varphi+\alpha_1+\alpha_2)\\ +\frac{M}{N}m_1 m_2 I_m\sin(\varphi+\alpha_1-\alpha_2)\end{bmatrix} \tag{26}$$

$$U_{a2\_\cos}=\frac{N}{96\omega_0 C}\begin{bmatrix}\frac{M}{N}48\omega_0 C m_2 U_{\rm cap}\sin\alpha_2\\ -9m_1 I_m\sin(\varphi-\alpha_1)\\ -4\frac{M}{N}m_2 i_{\rm dc}\cos\alpha_2-4m_1^2 i_{\rm dc}\sin 2\alpha_1\\ +3\frac{M}{N}m_1 m_2 I_m\cos(\varphi-\alpha_1-\alpha_2)\\ +\frac{M}{N}m_1 m_2 I_m\cos(\varphi+\alpha_1-\alpha_2)\end{bmatrix} \tag{27}$$

where $U_{\rm cap}$ is the dc component of capacitor voltage. Based on (10), (22), and (23), there is

$$2U_{a0}=U_{\rm dc}. \tag{28}$$

Combining (2), (5), (6), and (22)–(25), (29) can be obtained as

$$\begin{cases}U_{a1\_\sin}=U_e\cos\delta\\ U_{a1\_\cos}=U_e\sin\delta.\end{cases} \tag{29}$$

Due to circulating current suppression, the second-order components in u_{ua} and u_{la} are zero as

$$\begin{cases}U_{a2\_\sin}=0\\ U_{a2\_\cos}=0.\end{cases} \tag{30}$$

Equations (28)–(30) give an equation system with five unknown variables m_1, α_1, m_2, α_2, and $U_{\rm cap}$. At a given P and Q, these variables can be solved by numerical calculation. Afterward, the references (y_{j1}, y_{j2}) corresponding to (P, Q) can be obtained, as shown in Fig. 9.

B. Analysis of P and Q Region Under the Proposed Strategy

According to [24], the operation region of the MMC is theoretically limited by

$$P^2+Q^2\le {S_N}^2 \tag{31}$$

where S_N is the rated apparent power. Hence, the possible maximum PQ operating region of the MMC is a circle with the radius of 1.0 p.u., where the basis is S_N. On the other hand, the references (y_{j1}, y_{j2}) corresponding to (P, Q) also have to meet (32) so as to avoid overmodulation

$$\begin{cases}-1\le y_{j1}\le 1\\ -1\le y_{j2}\le 1\\ -1\le y_{euj}=-y_{j1}+y_{j2}\cdot M/N\le 1\\ -1\le y_{elj}=y_{j1}+y_{j2}\cdot M/N\le 1.\end{cases} \tag{32}$$

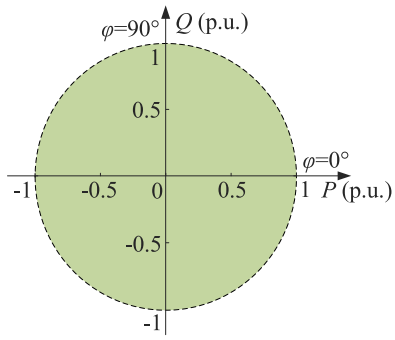

Fig. 10. Operation region of the MMC using the proposed strategy.

TABLE I
SIMULATION SYSTEM PARAMETERS

Parameter	Value
Rated apparent power S_N (MVA)	12
Grid line-to-line voltage (kV)	10
Grid frequency (Hz)	50
DC-link voltage U_{dc} (kV)	20
Number of SMs per arm N	10
SM capacitance C (mF)	8
Arm inductance L_s (mH)	6
Inductance L_f (mH)	2
Resistance R_f (mΩ)	1
Impedances (p.u.)	0.226
Total energy storage (kJ/MVA)	80

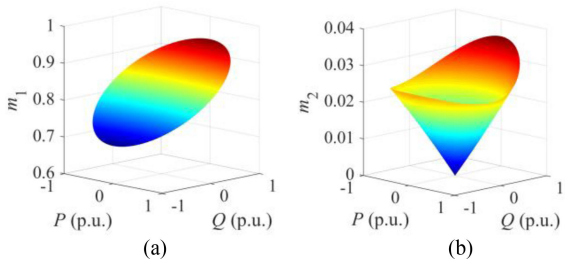

Fig. 11. Calculation results. (a) m_1. (b) m_2.

Based on Fig. 9, (31), and (32), the P and Q region of the MMC can be calculated, as shown in Fig. 10, which is based on the system parameters in Table I. Fig. 11 shows the amplitudes m_1 and m_2 of y_{j1} and y_{j2}, respectively. Here, the MMC can operate at the rated apparent power in the whole power factor angle range ($0\le\varphi\le 360^{\rm o}$).

VI. Comparison Between the Proposed Strategy and Strategy in [21]

A. Analysis of P and Q Region in [21]

Deng *et al.* [21] present control to suppress the dc-link high-frequency current ripple of the MMC under PD-PWM, where only one SM in each arm is used to suppress the circulating current and the others are used for power transmission. The SM equivalent references in the upper arm and the lower arm in [21]

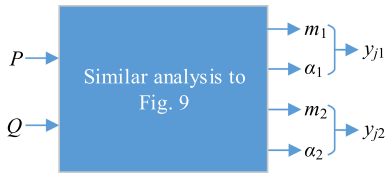

Fig. 12. Calculation for references y_{j1} and y_{j2} under the strategy in [21].

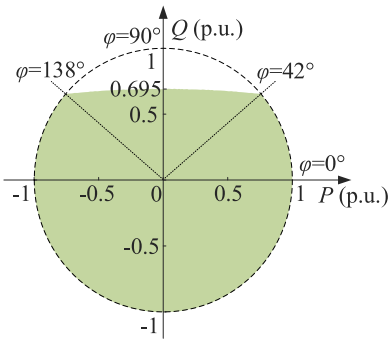

Fig. 13. Operating region of the MMC using the strategy in [21].

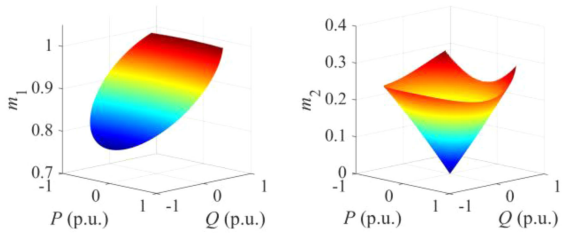

Fig. 14. Calculation results. (a) m_1. (b) m_2.

are as follows:

$$\begin{cases} y'_{euj} = -y_{j1} \cdot (N-1)/N + y_{j2}/N \\ y'_{elj} = y_{j1} \cdot (N-1)/N + y_{j2}/N. \end{cases} \tag{33}$$

Referring to the analysis between (P, Q) and (y_{j1}, y_{j2}) shown in Fig. 9 for the proposed strategy and replacing (18) with (33) in Section V-A, the relationship between (P, Q) and (y_{j1}, y_{j2}) in the strategy [21] can also be obtained, as shown in Fig. 12. Here, the references (y_{j1}, y_{j2}) corresponding to (P, Q) are limited by (34) so as to avoid the overmodulation, which may restrict the region of P and Q

$$\begin{cases} -1 \le y_{j1} \le 1 \\ -1 \le y_{j2} \le 1 \\ -1 \le y_{euj} = [-y_{j1} \cdot (N-1) + y_{j2}]/N \le 1 \\ -1 \le y_{elj} = [y_{j1} \cdot (N-1) + y_{j2}]/N \le 1. \end{cases} \tag{34}$$

Based on the above analysis, the P and Q region of the MMC using the strategy in [21] is calculated, as shown in Fig. 13, which is based on the system parameters in Table I. It shows that the MMC cannot operate at rated apparent power when $42° \le \varphi \le 138°$. The maximum reactive power that the MMC can output is only 0.695. Fig. 14 shows the amplitudes m_1 and m_2 of the references y_{j1} and y_{j2}, respectively. The operation region of the MMC is weakened under the strategy in [21].

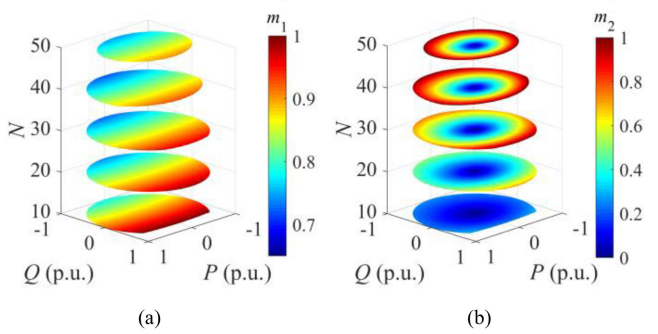

Fig. 15. P and Q region of MMCs using the strategy in [21] under various numbers of SMs per arm. (a) With m_1. (b) With m_2.

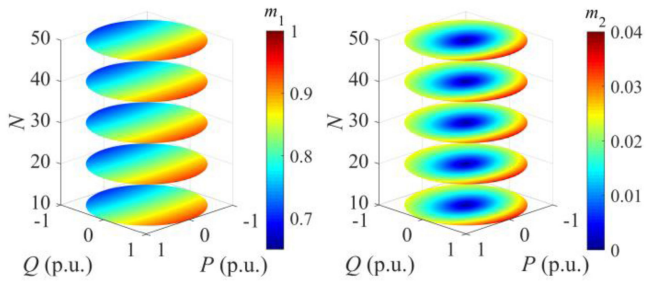

Fig. 16. P and Q region of MMCs using the proposed strategy under various numbers of SMs per arm. (a) With m_1. (b) With m_2.

B. Comparison Between the Proposed Strategy and [21]

According to the SM equivalent reference in (18), the ac EMF u_{ej} and the modulated second-order harmonic voltage u_{j2f} for suppressing second-order harmonic circulating current of the MMC under the proposed strategy are as follows:

$$\begin{cases} u_{ej} = y_{j1} \cdot U_{\rm dc}/2 \\ u_{j2f} = -y_{j2} \cdot U_{\rm dc} \cdot M/N. \end{cases} \tag{35}$$

According to the SM equivalent reference in (33), the ac EMF u'_{ej} and the modulated second-order harmonic voltage u'_{j2f} for suppressing second-order harmonic circulating current of MMCs under the strategy in [21] are as follows:

$$\begin{cases} u'_{ej} = y_{j1} \cdot \frac{N-1}{N} \frac{U_{\rm dc}}{2} \\ u'_{j2f} = -y_{j2} \cdot U_{\rm dc}/N. \end{cases} \tag{36}$$

According to (35) and (36), there is $u_{ej} > u'_{ej}$ and therefore the proposed strategy has wider operation range of the MMC in comparison with the strategy in [21]. In addition, the u_{ej} has nothing with the SM number N, whereas the u'_{ej} is decided by N. Along with the reduction of N, the u'_{ej} becomes small and the operation range of the MMC is reduced.

According to (35) and (36), u_{j2f} has little relationship with N, whereas u'_{j2f} is decided by N. Along with the increase of N, the u'_{j2f} becomes small. Consequently, the y_{j2} should be increased so as to maintain the u'_{j2f} to suppress the circulating current. However, y_{j2} has its limitation shown in (34), which restricts the operation region of the MMC.

Figs. 15 and 16 show the P and Q region of MMCs using the strategy in [21] and the proposed strategy, respectively, which

are calculated based on the system parameters in Table I. In Figs. 15 and 16, the MMC with different SM number per arm is considered including 10, 20, 30, 40, and 50, whereas the rated apparent power and dc-link voltage remain unchanged. In order to keep the same equivalent capacity discharging time constant [25], the SM capacitance is also changed proportionally.

Fig. 15(a) and (b) shows the P and Q region of the MMC corresponding to the modulation indexes m_1 and m_2 in y_{a1} and y_{a2}, respectively, under the strategy in [21]. The MMC almost cannot work at the rated apparent power in the whole power factor angle range under the strategy in [21], where the power operating region of the MMC varies under different numbers of SMs per arm. When N is close to 20, the MMC has a wider operating region. When $N < 20$, the maximum reactive power is reduced. When $N > 20$, the maximum reactive power and the maximum active power are both reduced.

Fig. 16(a) and (b) shows the P and Q region of the MMC corresponding to m_1 and m_2 in y_{a1} and y_{a2}, respectively, under the proposed strategy. Here, the MMC can work at the rated apparent power in the whole power factor angle range under the proposed strategy, which effectively expands the power region of the MMC in comparison with the strategy in [21].

VII. Simulation Studies

To verify the proposed strategy, a three-phase MMC system, as shown in Fig. 1, is simulated with PSCAD/EMTDC. The dc side of the MMC is connected to a dc voltage source. The circulating current suppression method [13] is adopted. The system parameters are listed in Table I.

A. With PD-PWM

Fig. 17 shows the performance of the MMC with PD-PWM, where $P = 1$ p.u. and $Q = 0$ at $\varphi = 0°$. The SM average switching frequency is 680 Hz. Fig. 17(a) shows the arm currents i_{ua}, i_{la}, and $(i_{ua} + i_{la})/2$ of phase A, where the second-order circulating current is suppressed. Fig. 17(b) shows the dc-link current, whose maximum peak-to-peak value is 22.8 A. Fig. 17(c)–(e) shows the total arm inductor voltages u_{sla}, u_{slb}, and u_{slc} in phases A, B, and C, respectively, which have voltage pulses as the theoretical analysis in Fig. 3. Fig. 17(f) shows the sum of total inductor voltages in phases A, B, and C, which causes the dc-link high-frequency current ripple, as shown in Fig. 17(g). Fig. 17(h) shows the spectrum of the dc-link current, which has many high-frequency components.

B. With the Proposed Strategy

Fig. 18 shows the performance of MMCs with the proposed strategy, where $P = 1$ p.u. and $Q = 0$ at $\varphi = 0°$. The SM average switching frequency is 780 Hz. Fig. 18(a) shows the arm current and circulating current $(i_{ua} + i_{la})/2$ of phase A. Fig. 18(b) shows the dc-link current $i_{\rm dc}$. The maximum peak-to-peak value of $i_{\rm dc}$ is only 3.2 A, which is less than one-seventh of that with PD-PWM in Fig. 17(b). Fig. 18(c) shows that the carriers' phase-shifting angles θ_{sa}, θ_{sb}, and θ_{sc} are in a small range between –0.32 and 0.18 in rad. Fig. 18(d)–(f) shows the inductor

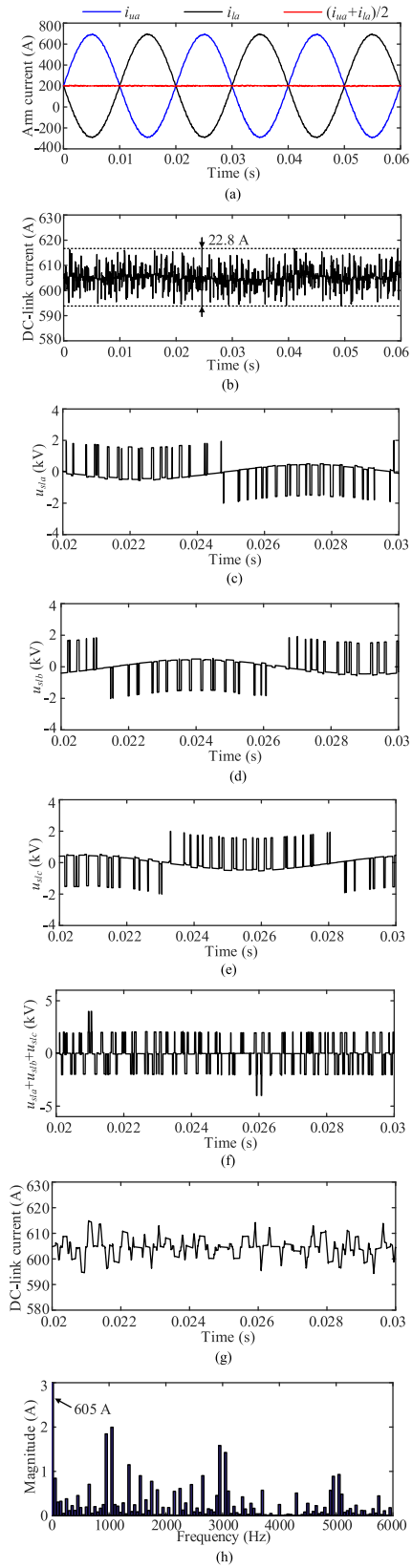

Fig. 17. Simulation waveforms using PD-PWM. (a) i_{ua}, i_{la}, and $(i_{ua} + i_{la})/2$ in phase A. (b) DC-link current. (c) Arm inductor voltage u_{sla}. (d) Arm inductor voltage u_{slb}. (e) Arm inductor voltage u_{slc}. (f) Sum of u_{sla}, u_{slb}, and u_{slc}. (g) DC-link current. (h) Spectrum of dc-link current.

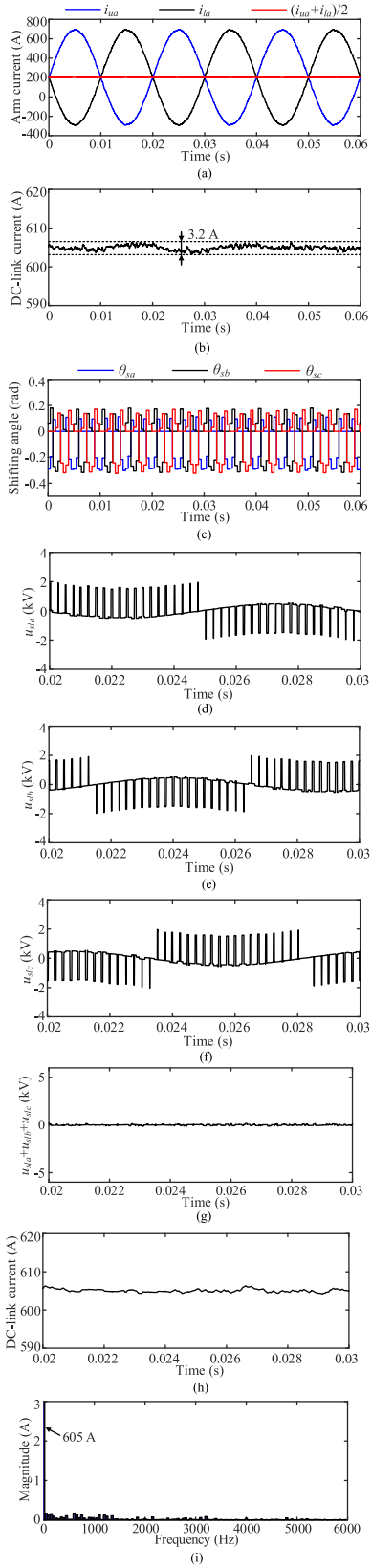

Fig. 18. Simulation waveforms using the proposed strategy. (a) i_{ua}, i_{la}, and $(i_{ua}+i_{la})/2$ in phase A. (b) DC-link current. (c) Carriers' phase-shifting angles θ_{sa}, θ_{sb}, and θ_{sc}. (d) Arm inductor voltage u_{sla}. (e) Arm inductor voltage u_{slb}. (f) Arm inductor voltage u_{slc}. (g) Sum of u_{sla}, u_{slb}, and u_{slc}. (h) DC-link current. (i) Spectrum of dc-link current.

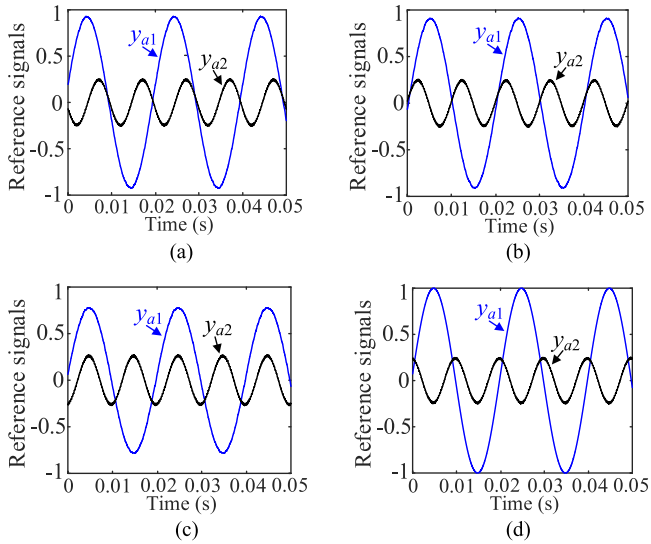

Fig. 19. References y'_{a1} and y'_{a2}. (a) $\varphi = 0°$ ($P = 1.0$ p.u., $Q = 0$). (b) $\varphi = 180°$ ($P = -1.0$ p.u., $Q = 0$). (c) $\varphi = 270°$ ($P = 0$, $Q = -1.0$ p.u.). (d) $\varphi = 90°$ ($P = 0$, $Q = 0.699$ p.u.).

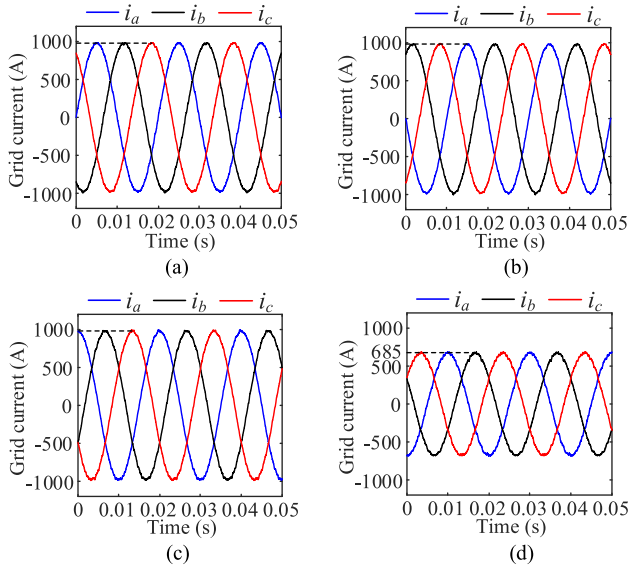

Fig. 20. Grid current under [21]. (a) $\varphi = 0°$ ($P = 1.0$ p.u., $Q = 0$). (b) $\varphi = 180°$ ($P = -1.0$ p.u., $Q = 0$). (c) $\varphi = 270°$ ($P = 0$, $Q = -1.0$ p.u.). (d) $\varphi = 90°$ ($P = 0$, $Q = 0.699$ p.u.).

voltages u_{sla}, u_{slb}, and u_{slc}, respectively. With the proposed strategy, the sum of u_{sla}, u_{slb}, and u_{slc} is nearly zero in Fig. 18(g), which eliminates high-frequency current ripple in the $i_{\rm dc}$, as shown in Fig. 18(h). Fig. 18(i) shows the spectrum of the $i_{\rm dc}$. Compared with Fig. 17(h), the high-frequency components are much reduced with the proposed strategy.

C. P and Q Region in Strategy [21] and the Proposed Strategy

Figs. 19 and 20 show the performance of the MMC using the strategy in [21]. Fig. 19 shows the references y_{a1} and y_{a2} for the MMC in four operation conditions. Fig. 19(a) shows y_{a1} and y_{a2} when the MMC outputs rated active power $P = 1$ p.u. at $\varphi = 0°$. Fig. 19(b) shows y_{a1} and y_{a2} when the MMC absorbs

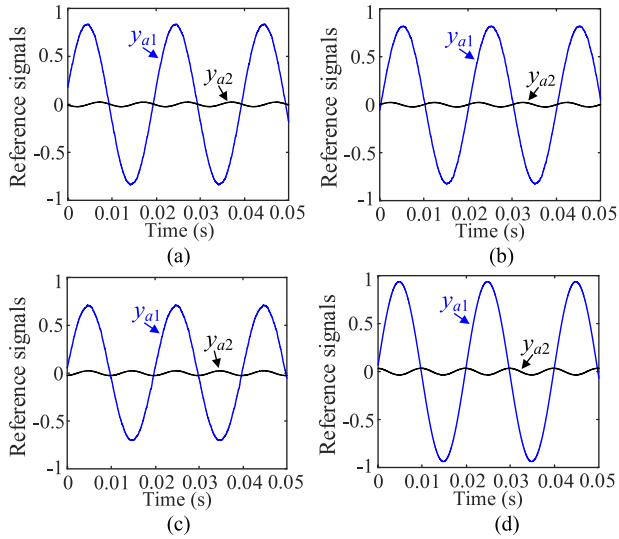

Fig. 21. References y_{a1} and y_{a2}. (a) $\varphi = 0°$, $P = 1.0$ p.u., $Q = 0$. (b) $\varphi = 180°$, $P = –1.0$ p.u., $Q = 0$. (c) $\varphi = 270°$, $P = 0$, $Q = –1.0$ p.u.. (d) $\varphi = 90°$, $P = 0$, $Q = 1.0$ p.u.

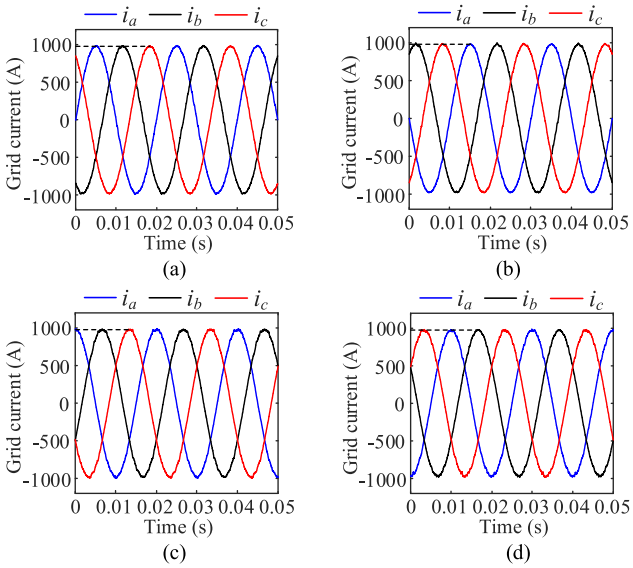

Fig. 22. Grid current under the proposed strategy. (a) $\varphi = 0°$ ($P = 1.0$ p.u., $Q = 0$). (b) $\varphi = 180°$ ($P = –1.0$ p.u., $Q = 0$). (c) $\varphi = 270°$ ($P = 0$, $Q = –1.0$ p.u.). (d) $\varphi = 90°$ ($P = 0$, $Q = 1.0$ p.u.).

active power $P = –1$ p.u. at $\varphi = 180°$. Fig. 19(c) shows y_{a1} and y_{a2} when the MMC absorbs reactive power $Q = –1$ p.u. at $\varphi = 270°$. The MMC can work at the rated apparent power when φ is 0°, 180°, and 270°, respectively. Fig. 19(d) shows y_{a1} and y_{a2} when the MMC outputs maximum reactive power at $\varphi = 90°$. Here, the maximum reactive power is only 0.699 p.u., though y_{a1} reaches its maximum value of 1.0. Fig. 20(a)–(d) shows the grid current for the above four conditions. The amplitude drops to 685 A at $\varphi = 90°$, which is about 69.9% of the rated value (980 A).

Figs. 21 and 22 show the performance of the MMC using the proposed strategy. Fig. 21(a)–(d) shows the references y_{a1} and y_{a2} in four conditions including at $P = 1$ p.u. and $Q = 0$, at $P = –1$ p.u. and $Q = 0$, at $P = 0$ and $Q = –1$ p.u., and at $P = 0$ and $Q = 1$ p.u., where the MMC can work at the rated apparent power when φ is 0°, 180°, 270°, and 90°, respectively. Fig. 22(a)–(d) shows the grid current for the above four conditions. The amplitudes are all nearly the same and equal to the rated value.

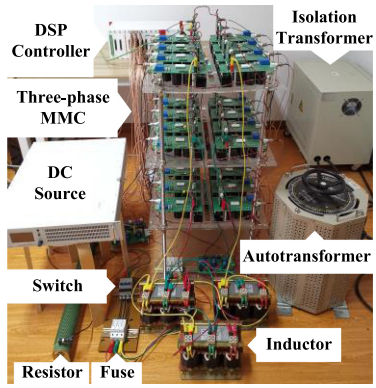

Fig. 23. Photograph of the experimental setup.

TABLE II
EXPERIMENTAL SYSTEM PARAMETERS

Parameter	Value
Rated Apparent Power S_N (kVA)	1
DC-link voltage U_{dc} (V)	200
Voltage at MMC side of AT (V)	85
Rated frequency (Hz)	50
SM Number per arm	4
Inductance L_s (mH)	5
Capacitance C (mF)	2.35
Inductance L_f (mH)	5
Carrier frequency f_c (kHz)	2
Impedances (p.u.)	0.22
Total energy storage (kJ/MVA)	70.5

VIII. EXPERIMENTAL STUDIES

A three-phase MMC prototype is built in the laboratory to verify the proposed strategy. Fig. 23 shows the photograph of the experimental setup. A dc power supply paralleled with the resistor is used to support the dc-link voltage. The ac side of the MMC is connected to the grid via an isolation transformer and an autotransformer. The control algorithm is implemented by digital signal processor (DSP) and the drive signals are transferred to the driving panel of each SM by optical fibers. The system parameters are listed in Table II.

A. With PD-PWM

Fig. 24 shows the performance of MMCs with PD-PWM, where the SM average switching frequency is 1090 Hz. Fig. 24(a) shows the upper and lower arm currents i_{ua}, i_{la}, and $i_{ua} + i_{la}$. Fig. 24(b) shows the upper arm currents i_{ua}, i_{ub}, and i_{uc} in phases A, B, and C and the dc-link current $i_{\rm dc}$, where the maximum dc-link current ripple is 4.9 A. Fig. 24(c) shows the total inductor voltages u_{sla}, u_{slb}, and u_{slc} in phases A, B, and C, as well as the caused dc-link current ripple. Fig. 24(d) shows u_{sla}, u_{slb}, u_{slc}, and $i_{\rm dc}$ in a small time scale. There are

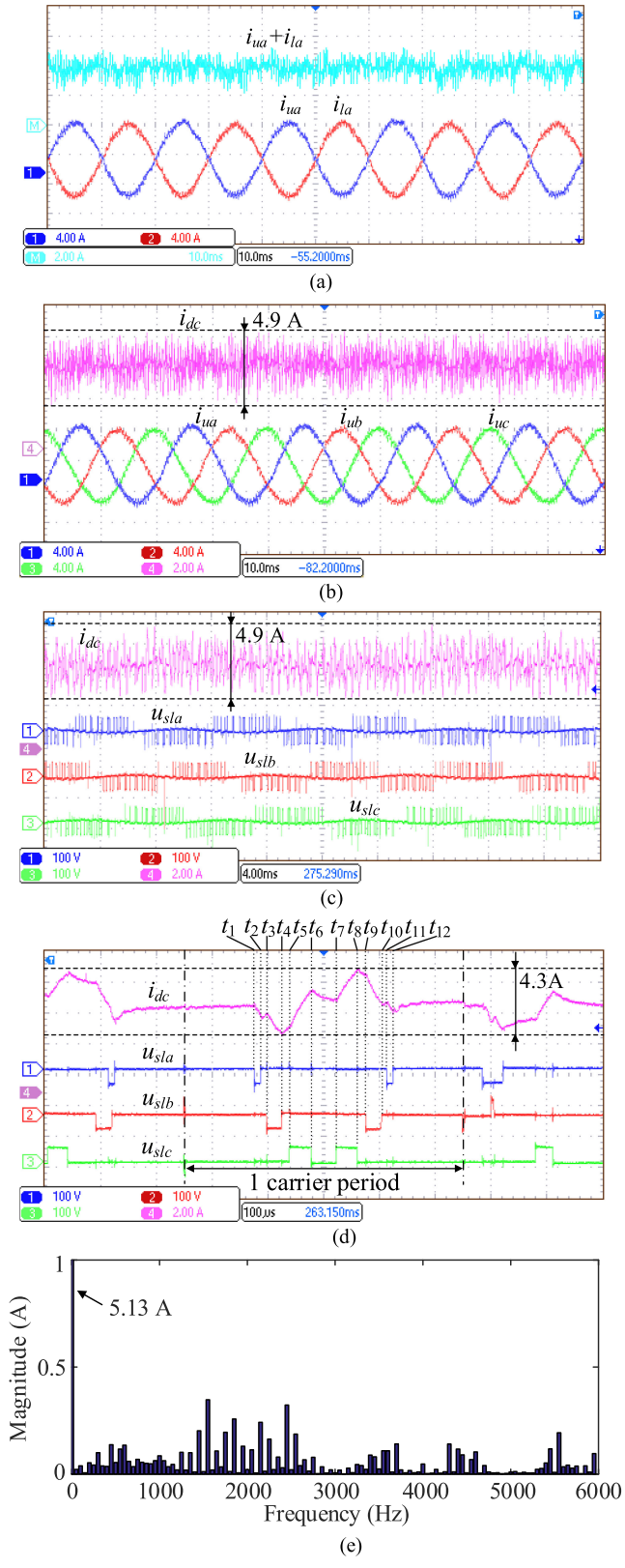

Fig. 24. Experimental waveforms with PD-PWM. (a) i_{ua}, i_{ub} (4 A/div), and $i_{ua}+i_{ub}$ (2 A/div). Time base is 10 ms. (b) i_{ua}, i_{ub}, i_{uc} (4 A/div), and $i_{\rm dc}$ (2 A/div). Time base is 10 ms. (c) u_{sla}, u_{slb}, u_{slc} (100 V/div), and $i_{\rm dc}$ (2 A/div). Time base is 4 ms. (d) u_{sla}, u_{slb}, u_{slc} (100 V/div), and $i_{\rm dc}$ (2 A/div). Time base is 100 μs. (e) Spectrum of the dc-link current.

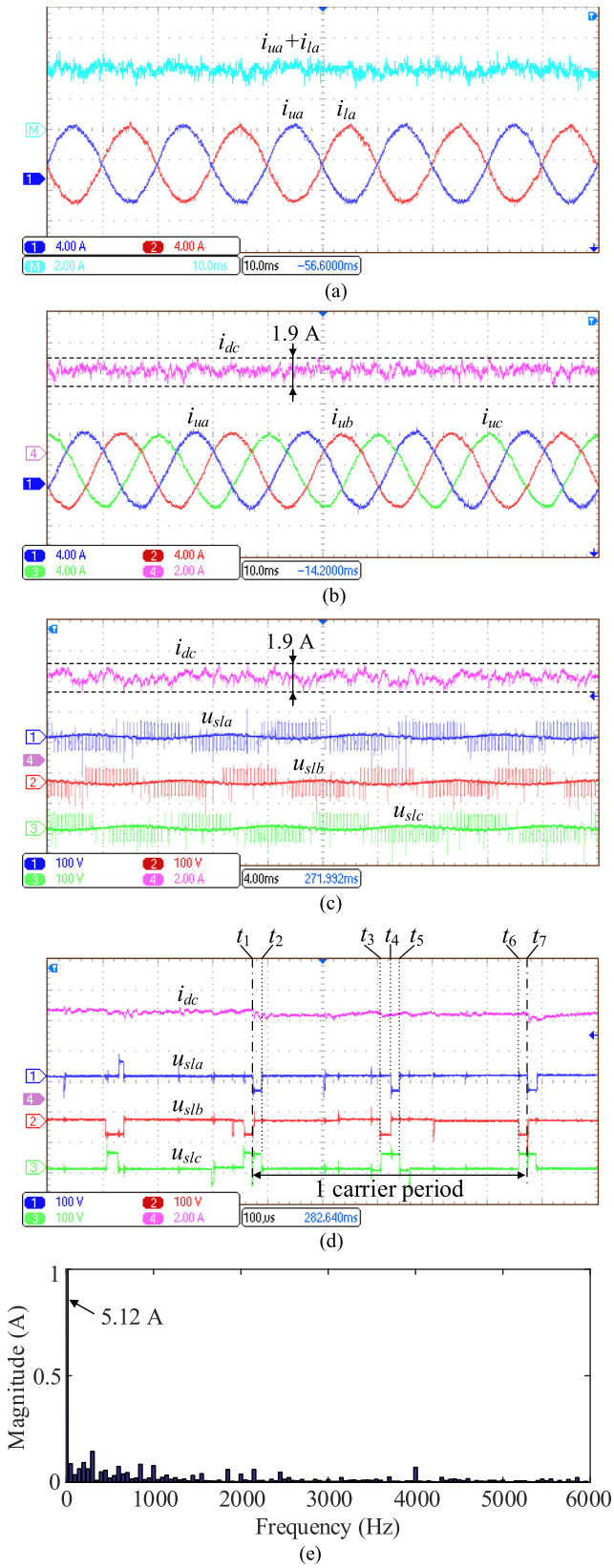

Fig. 25. Experimental waveforms with proposed strategy. (a) i_{ua}, i_{ub} (4 A/div), and $i_{ua}+i_{ub}$ (2 A/div). Time base is 10 ms. (b) i_{ua}, i_{ub}, i_{uc} (4 A/div), and $i_{\rm dc}$ (2 A/div). Time base is 10 ms. (c) u_{sla}, u_{slb}, u_{slc} (100 V/div), and $i_{\rm dc}$ (2 A/div). Time base is 4 ms. (d) u_{sla}, u_{slb}, u_{slc} (100 V/div), and $i_{\rm dc}$ (2 A/div). Time base is 100 μs. (e) Spectrum of the dc-link current.

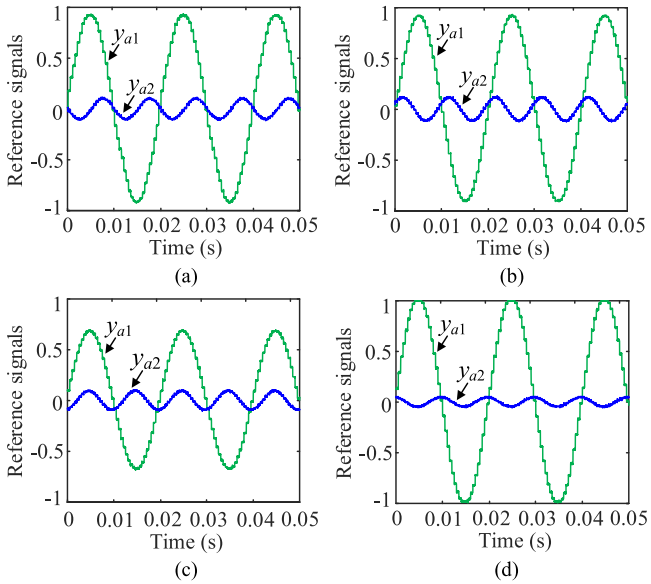

Fig. 26. Experimental waveforms of reference signals y_{a1} and y_{a2} with the strategy in [21]. (a) $\varphi = 0°$ ($P = 1.0$ p.u., $Q = 0$). (b) $\varphi = 180°$ ($P = –1.0$ p.u., $Q = 0$). (c) $\varphi = 270°$ ($P = 0$, $Q = –1.0$ p.u.). (d) $\varphi = 90°$ ($P = 0$, $Q = 0.32$ p.u.).

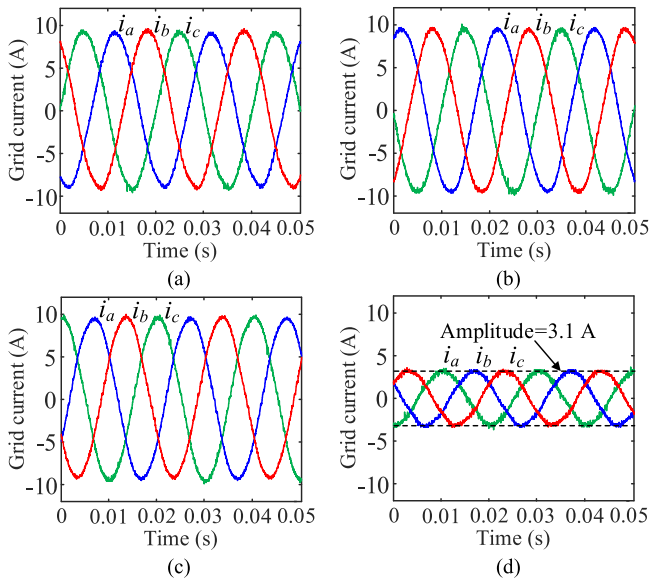

Fig. 27. Experimental waveforms of grid current with the strategy in [21]. (a) $\varphi = 0°$ ($P = 1.0$ p.u., $Q = 0$). (b) $\varphi = 180°$ ($P = –1.0$ p.u., $Q = 0$). (c) $\varphi = 270°$ ($P = 0$, $Q = –1.0$ p.u.). (d) $\varphi = 90°$ ($P = 0$, $Q = 0.32$ p.u.).

several voltage pulses in each carrier period, which cause the ripple of $i_{\rm dc}$. $i_{\rm dc}$ drops in the periods t_1–t_2, t_3–t_4, t_9–t_{10}, t_{11}–t_{12} due to the negative pulses of u_{sla} and u_{slb} and rises in the periods t_5–t_6, t_7–t_8 because of the positive pulses of u_{slc}. As a result, the peak-to-peak value of $i_{\rm dc}$ reaches 4.3 A. Fig. 17(e) shows the spectrum of $i_{\rm dc}$.

B. With the Proposed Strategy

Fig. 25 shows the performance of the MMC using the proposed strategy, where the SM average switching frequency is 1310 Hz. Fig. 25(a) shows the i_{ua}, i_{la}, and $i_{ua} + i_{la}$ in phase A. Fig. 25(b) shows the upper arm currents i_{ua}, i_{ub}, i_{uc} in phases A, B, and C and $i_{\rm dc}$. The maximum ripple of $i_{\rm dc}$ is 1.9 A, which is only 38.8% of that in Fig. 24(b). Fig. 25(c) shows the inductor voltages u_{sla}, u_{slb}, and u_{slc} in phases A, B, and C, as well as the caused dc-link current ripple. Fig. 25(d) shows the u_{sla}, u_{slb}, u_{slc}, and $i_{\rm dc}$ in small time scale. It can be observed that u_{sla}, u_{slb}, and u_{slc} in three phases are phase shifted and the sum is almost zero in each carrier period, which eliminates the high-frequency ripple for $i_{\rm dc}$. Fig. 25(e) shows the spectrum of the dc-link current, where the high-frequency components are much reduced in comparison with Fig. 24(e).

C. P and Q Region for Strategy in [21] and the Proposed Strategy

Fig. 26 shows the measured fundamental frequency component and second-order component of the references for phase A using the strategy in [21]. Fig. 26(a)–(c) shows the references when $\varphi = 0°$, 180°, and 270°, respectively. The MMC works, respectively, at: 1) $P = 1.0$ p.u., $Q = 0$, 2) $P = –1.0$ p.u., $Q = 0$, and 3) $P = 0$, $Q = –1.0$ p.u. Fig. 26(d) shows the references when the MMC outputs maximum reactive power at $\varphi = 90°$. The maximum reactive power, however, is only 0.32 p.u., though y'_{a1} reaches its maximum value 1.0. Fig. 27 shows the grid current for the above four conditions. The amplitude of the grid current at $\varphi = 90°$ drops to 3.1 A, which is about 32% of the rated value (9.6 A).

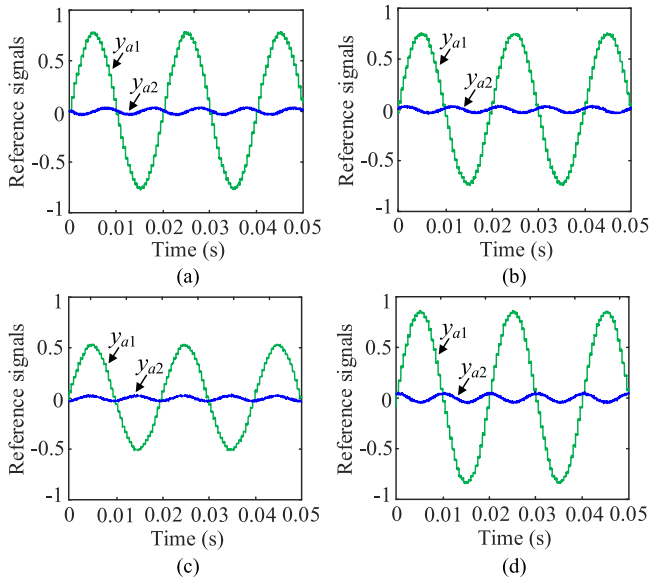

Fig. 28. Experimental waveforms of reference signals y_{a1} and y_{a2} with the proposed strategy. (a) $\varphi = 0°$ ($P = 1.0$ p.u., $Q = 0$). (b) $\varphi = 180°$ ($P = –1.0$ p.u., $Q = 0$). (c) $\varphi = 270°$ ($P = 0$, $Q = –1.0$ p.u.). (d) $\varphi = 90°$ ($P = 0$, $Q = 1.0$ p.u.).

Fig. 28 shows the measured fundamental frequency component and second-order component of the references for phase A using the proposed strategy. Fig. 28(a)–(d) shows the references when $\varphi = 0°$, 180°, 270°, and 90°, respectively. The MMC works, respectively, at 1) $P = 1.0$ p.u., $Q = 0$, 2) $P = –1.0$ p.u., $Q = 0$, 3) $P = 0$, $Q = –1.0$, and 4) $P = 0$, $Q = 1.0$. Fig. 29 shows

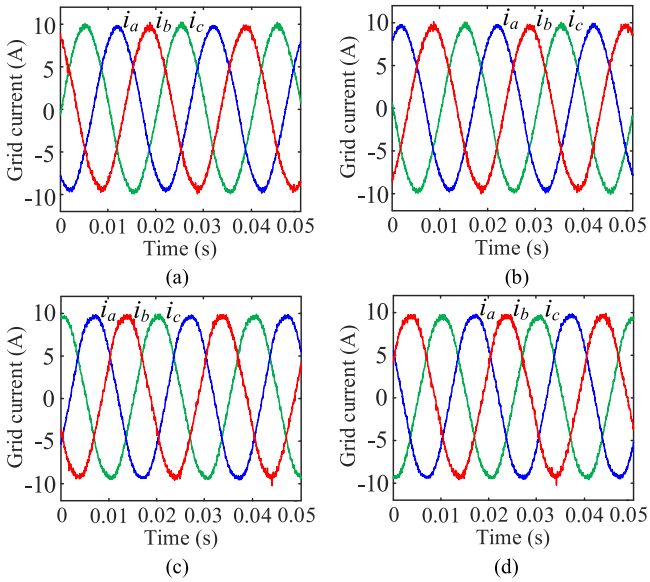

Fig. 29. Experimental waveforms of grid current with the proposed strategy. (a) $\varphi = 0°$ ($P = 1.0$ p.u., $Q = 0$). (b) $\varphi = 180°$ ($P = -1.0$ p.u., $Q = 0$). (c) $\varphi = 270°$ ($P = 0$, $Q = -1.0$ p.u.). (d) $\varphi = 90°$ ($P = 0$, $Q = 1.0$ p.u.).

the grid current for the above four conditions. With proposed strategy, the MMC can operate at rated apparent power, which extends the power region in comparison with [21].

IX. Conclusion

This article proposes a phase-shifted DGM-based PD-PWM strategy for MMCs. The fundamental frequency component and the second-order component of the arm reference are modulated separately by different groups of carriers, respectively. By shifting the phase angles of the carriers in each carrier period, the high-frequency current in the arms caused by the active circulating current suppression can be counteracted for three phases so that the dc-link high-frequency current ripple can be eliminated. Besides, the proposed strategy overcomes the operation region reduction, so that the MMC with the proposed strategy has a wider operation region in comparison with the existing dc-link current ripple suppression strategy under PD-PWM. Simulations and experimental studies are conducted and demonstrate the effectiveness of the proposed strategy.

References

[1] M. Huang, J. Zou, and X. Ma, "An improved phase-shifted carrier modulation for modular multilevel converter to suppress the influence of fluctuation of capacitor voltage," *IEEE Trans. Power Electron.*, vol. 31, no. 10, pp. 7404–7416, Oct. 2016.

[2] O. S. H. M. Abushafa, M. S. A. Dahidah, S. M. Gadoue, and D. J. Atkinson, "Submodule voltage estimation scheme in modular multilevel converters with reduced voltage sensors based on Kalman filter approach," *IEEE Trans. Ind. Electron.*, vol. 65, no. 9, pp. 7025–7035, Sep. 2018.

[3] Y. Luo, Z. Li, L. Xu, X. Xiong, Y. Li, and C. Zhao, "An adaptive voltage-balancing method for high-power modular multilevel converters," *IEEE Trans. Power Electron.*, vol. 33, no. 4, pp. 2901–2912, Apr. 2018.

[4] F. Deng, Y. Lv, C. Liu, Q. Heng, Q. Yu, and J. Zhao, "Overview on submodule topologies, modeling, modulation, control schemes, fault diagnosis and tolerant control strategies of modular multilevel converters," *Chin. J. Elect. Eng.*, vol. 6, no. 1, pp. 1–21, Mar. 2020.

[5] F. Deng, C. Liu, Q. Wang, R. Zhu, X. Cai, and Z. Chen, "A currentless submodule individual voltage balancing control for modular multilevel converters," *IEEE Trans. Ind. Electron.*, vol. 67, no. 11, pp. 9370–9382, Nov. 2020.

[6] S. Debnath, J. Qin, B. Bahrani, M. Saeedifard, and P. Barbosa, "Operation, control, and applications of the modular multilevel converter: A review," *IEEE Trans. Power Electron.*, vol. 30, no. 1, pp. 37–53, Jan. 2015.

[7] J. Li, G. Konstantious, H. R. Wickramasinghe, and J. Pou, "Operation and control methods of modular multilevel converters in unbalanced ac grids: A review," *IEEE J. Emerg. Sel. Topics Power Electron.*, vol. 7, no. 2, pp. 1258–1271, Jun. 2019.

[8] X. Chen, J. Liu, S. Song, and S. Ouyang, "Circulating harmonic currents suppression of level-increased NLM based modular multilevel converter with deadbeat control," *IEEE Trans. Power Electron.*, vol. 35, no. 11, pp. 11418–11429, Nov. 2020.

[9] S. Zhou, B. Li, M. Guan, X. Zhang, Z. Xu, and D. Xu, "Capacitance reduction of the hybrid modular multilevel converter by decreasing average capacitor voltage in variable-speed drives," *IEEE Trans. Power Electron.*, vol. 34, no. 2, pp. 1580–1594, Feb. 2019.

[10] P. Hu and D. Jiang, "A level-increased nearest level modulation method for modular multilevel converters," *IEEE Trans. Power Electron.*, vol. 30, no. 4, pp. 1836–1842, Apr. 2015.

[11] D. Wu and L. Peng, "Analysis and suppressing method for the output voltage harmonics of modular multilevel converter," *IEEE Trans. Power Electron.*, vol. 31, no. 7, pp. 4755–4765, Jan. 2016.

[12] S. Yang, P. Wang, Y. Tang, M. Zagrodnik, X. Hu, and K. J. Tseng, "Circulating current suppression in modular multilevel converters with even-harmonic repetitive control," *IEEE Trans. Ind. Appl.*, vol. 54, no. 1, pp. 298–309, Jan./Feb. 2018.

[13] Q. Tu, Z. Xu, and L. Xu, "Reduced switching-frequency modulation and circulating current suppression for modular multilevel converters," *IEEE Trans. Power Del.*, vol. 26, no. 3, pp. 2009–2017, Jul. 2011.

[14] Q. Tu, Z. Xu, Y. Chang, and L. Guan, "Suppressing dc voltage ripples of MMC-HVDC under unbalanced grid conditions," *IEEE Trans. Power Del.*, vol. 27, no. 3, pp. 1332–1338, Jul. 2012.

[15] J. Wang, J. Liang, C. Wang, and X. Dong, "Circulating current suppression for MMC-HVDC under unbalanced grid conditions," *IEEE Trans. Ind. Appl.*, vol. 53, no. 4, pp. 3250–3259, Jul./Aug. 2017.

[16] A. Dekka, B. Wu, and N. R. Zargari, "Minimization of dc-bus current ripple in modular multilevel converter under unbalanced conditions," *IEEE Trans. Power Electron.*, vol. 32, no. 6, pp. 4125–4131, Jun. 2017.

[17] F. Deng and Z. Chen, "A control method for voltage balancing in modular multilevel converters," *IEEE Trans. Power Electron.*, vol. 29, no. 1, pp. 66–76, Jan. 2014.

[18] F. Deng and Z. Chen, "Elimination of dc-link current ripple for modular multilevel converters with capacitor voltage balancing pulse-shifted carrier PWM," *IEEE Trans. Power Electron.*, vol. 30, no. 1, pp. 284–296, Jan. 2015.

[19] Y. Li, E. A. Jones, and F. Wang, "Circulating current suppressing control's impact on arm inductance selection for modular multilevel converter," *IEEE J. Emerg. Sel. Topics Power Electron.*, vol. 5, no. 1, pp. 182–188, Mar. 2017.

[20] K. Li, Y. Liao, H. Lin, R. Lin, and J. Zhang, "Circulating current suppression with improved dc-link power quality for modular multilevel converter," *IET Gener. Transmiss. Distrib.*, vol. 12, no. 10, pp. 2220–2230, Apr. 2018.

[21] F. Deng, Q. Yu, Q. Wang, R. Zhu, X. Cai, and Z. Chen, "Suppression of dc-link current ripple for modular multilevel converters under phase-disposition PWM," *IEEE Trans. Power Electron.*, vol. 35, no. 3, pp. 3310–3324, Mar. 2020.

[22] B. Li, Z. Xu, S. Shi, D. Xu, and W. Wang, "Comparative study of the active and passive circulating current suppression methods for modular multilevel converters," *IEEE Power Electron. Lett.*, vol. 33, no. 3, pp. 1878–1883, Mar. 2018.

[23] T. Sakamoto and N. Hori, "New PWM schemes based on the principle of equivalent areas," in *Proc. IEEE Int. Symp. Ind. Electron.*, L'Aquila, Italy, 2002, pp. 505–510.

[24] Q. Song, W. Yang, B. Zhao, J. Meng, S. Xu, and Z. Zhu, "Low-capacitance modular multilevel converter operating with high capacitor voltage ripples," *IEEE Trans. Ind. Electron.*, vol. 66, no. 10, pp. 7456–7467, Oct. 2019.

[25] Z. Xu, H. Xiao, and Z. Zhang, "Selection methods of main circuit parameters for modular multilevel converters," *IET Renewable Power Gener.*, vol. 10, no. 6, pp. 788–797, Jun. 2018.

Qiang Yu received the B.Eng. degree in electrical engineering from Jilin University, Changchun, China, in 2017. He is currently working toward the Ph.D. degree with the School of Electrical Engineering, Southeast University, Nanjing, China.

His research interests include modular multilevel converters and high-voltage direct current technology.

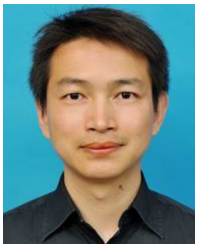

Fujin Deng (Senior Member, IEEE) received the B.Eng. degree in electrical engineering from China University of Mining and Technology, Xuzhou, China, in 2005, the M.Sc. degree in electrical engineering from Shanghai Jiao Tong University, Shanghai, China, in 2008, and the Ph.D. degree in energy technology from the Department of Energy Technology, Aalborg University, Aalborg, Denmark, in 2012.

In 2017, he joined the School of Electrical Engineering, Southeast University, Nanjing, China, as a Professor. From 2013 to 2015 and from 2015 to 2017, he was a Postdoctoral Researcher and an Assistant Professor, respectively, with the Department of Energy Technology, Aalborg University. His research interests include wind power generation, multilevel converters, high-voltage direct-current technology, dc grid, and offshore wind farm-power systems dynamics.

Chengkai Liu was born in Fujian, China, in 1996. He received the B.Eng. degree in electrical engineering from Chien-Shiung WU College, Southeast University, Nanjing, China, in 2018. He is currently working toward the Ph.D. degree with the School of Electrical Engineering, Southeast University.

His research interests include multilevel converters and dc grids.

Jifeng Zhao received the B.Eng. and M.Sc. degrees in electrical engineering from China University of Mining and Technology, Xuzhou, China, in 2015 and 2018, respectively. He is currently working toward the Ph.D. degree with the School of Electrical Engineering, Southeast University, Nanjing, China.

His research interests include multilevel converters and high-voltage direct-current technology.

Frede Blaabjerg received honoris causa from University Politehnica Timisoara (UPT), Romania, in 2017, and Tallinn Technical University (TTU) in Estonia, 2018.

From 1987 to 1988, he was with ABB-Scandia, Randers, Denmark. He became an Assistant Professor in 1992, an Associate Professor in 1996, and a Full Professor of power electronics and drives in 1998. In 2017, he became a Villum Investigator. He has authored/coauthored more than 600 journal papers in the fields of power electronics and its applications. He is the co-author of four monographs and editor of ten books in power electronics and its applications. His research interests include power electronics and its applications such as in wind turbines, PV systems, reliability, harmonics, and adjustable speed drives.

Dr. Blaabjerg was the recipient of 32 IEEE Prize Paper Awards, the IEEE PELS Distinguished Service Award in 2009, the EPE-PEMC Council Award in 2010, the IEEE William E. Newell Power Electronics Award 2014, the Villum Kann Rasmussen Research Award 2014, the Global Energy Prize in 2019, and the 2020 IEEE Edison Medal. He was the Editor-in-Chief for the IEEE TRANSACTIONS ON POWER ELECTRONICS from 2006 to 2012. He was the Distinguished Lecturer for the IEEE Power Electronics Society from 2005 to 2007 and for the IEEE Industry Applications Society from 2010 to 2011 as well as from 2017 to 2018. From 2019 to 2020, he was the President of IEEE Power Electronics Society. He is also the Vice-President of the Danish Academy of Technical Sciences. From 2014 to 2019, he was nominated by Thomson Reuters to be between the 250 cited most-researchers in engineering in the world.

Sayed Abulanwar (Member, IEEE) received the B.Sc. and M.Sc. degrees in electrical engineering from Mansoura University, Mansoura, Egypt, in 2005 and 2010, respectively, and the Ph.D. degree from Aalborg University, Aalborg, Denmark, in 2016.

He is currently an Assistant Professor of electrical engineering with Mansoura University. His research interests include wind turbine control, high-voltage direct-current systems, and transients in power systems.